The KLOE electromagnetic calorimeter

M. Adinolfi[a], F. Ambrosino[b], A. Antonelli[c], M. Antonelli[c], F. Anulli[c],
G. Barbiellini[d], G. Bencivenni[c], S. Bertolucci[c], C. Bini[e,*], C. Bloise[c],
V. Bocci[e], F. Bossi[c], P. Branchini[f,1], G. Cabibbo[e], R. Caloi[e], P. Campana[c],
M. Casarsa[d], G. Cataldi[g,2], F. Ceradini[f], F. Cervelli[h], P. Ciambrone[c],
E. De Lucia[e], P. De Simone[c], G. De Zorzi[e], S. Dell'Agnello[c], A. Denig[c,2],
A. Di Domenico[e], C. Di Donato[b], S. Di Falco[h], A. Doria[b], O. Erriquez[i],
A. Farilla[f], A. Ferrari[f], M.L. Ferrer[c], G. Finocchiaro[c], C. Forti[c],
A. Franceschi[c], P. Franzini[e,j], M.L. Gao[c,k], C. Gatti[c], P. Gauzzi[e], A. Giannasi[h],
S. Giovannella[c], E. Graziani[f,1], H.G. Han[c,k], S.W. Han[c,k], X. Huang[c,k],
M. Incagli[h], L. Ingrosso[c], L. Keeble[c], W. Kim[l], C. Kuo[m], G. Lanfranchi[c],
J. Lee-Franzini[c,l], T. Lomtadze[h], C.S. Mao[c,k], M. Martemianov[c,n], W. Mei[c],
R. Messi[a], S. Miscetti[c], S. Moccia[c], M. Moulson[c], S. Müller[m], F. Murtas[c],
L. Pacciani[a], M. Palomba[h], M. Palutan[f], E. Pasqualucci[e], L. Passalacqua[c],
A. Passeri[f,1], D. Picca[e], G. Pirozzi[b], L. Pontecorvo[e], M. Primavera[g],
P. Santangelo[c], E. Santovetti[a], G. Saracino[b], R.D. Schamberger[l],
B. Sciascia[e], F. Scuri[d], I. Sfiligoi[c], P. Silano[e], T. Spadaro[e], E. Spiriti[f,1],
L. Tortora[f,1], P. Valente[c], B. Valeriani[m], G. Venanzoni[h,2], A. Ventura[g],
S. Wölfle[c], Y. Wu[c,k], Y.G. Xie[c,k], P.F. Zema[h], C.D. Zhang[c,k],
J.Q. Zhang[c,k], P.P. Zhao[c,k]

[a] Departimento di Fisica dell'Università e Sezione INFN, Roma II, Italy
[b] Dipartimento di Scienze Fisiche dell'Università e Sezione INFN, Napoli, Italy
[c] Laboratori Nazionali di Frascati dell'INFN, Frascati, Italy
[d] Dipartimento di Fisica dell'Università e Sezione INFN, Trieste, Italy
[e] Cesare Bini Dipartimento di Fisica Università "La Sapienza" P.le A. Moro 5 00185 Roma, Italy
[f] Dipartimento di Fisica dell'Università e Sezione INFN, Roma III, Italy
[g] Departimento di Fisica dell'Università e Sezione INFN, Lecce, Italy
[h] Departimento di Fisica dell'Università e Sezione INFN, Pisa, Italy
[i] Dipartimento di Fisica dell'Università e Sezione INFN, Bari, Italy
[j] Physics Department, Columbia University, New York, USA
[k] Permanent address: Institute of High Energy Physics of Academica Sinica, Beijing, China
[l] Physics Department, State University of New York at Stony Brook, USA

*Corresponding author. Tel.: +39-06-4991-4266.
E-mail address: cesare.bini@roma1.infn.it (C. Bini).
[1] Formerly Istituto Superiore di Sanità and Sezione INFN, ISS, Roma, Italy.
[2] Formerly Institut für Experimentelle Kernphysik, Universität Karlsruhe, Germany.

[m] *Institut für Experimentelle Kernphysik, Universität Karlsruhe, Germany*
[n] *Permanent address: Institute for Theoretical and Experimental Physics, Moscow, Russia*

Abstract

The KLOE detector was designed primarily for the study of CP violation in neutral kaon decays at DAΦNE, the Frascati φ-factory. The detector consists of a tracker and an electromagnetic calorimeter. A lead-scintillating-fiber sampling calorimeter satisfies best the requirements of the experiment, providing adequate energy resolution and superior timing accuracy. We describe in the following the construction of the calorimeter, its calibration and how the calorimeter information is used to obtain energy, point of entry and time of the arrival of photons, electrons and charged particles. With e^+e^- collision data at DAΦNE for an integrated luminosity of some 2 pb^{-1} we find for electromagnetic showers, an energy resolution of $5.7\%/\sqrt{E(\text{GeV})}$ and a time resolution of $54/\sqrt{E(\text{GeV})}$ ps. We also present a measurement of efficiency for low energy photons. © 2002 Elsevier Science B.V. All rights reserved.

1. Introduction

The KLOE detector [1,2], primarily designed for the study of CP violation in the decays of neutral kaons, [1] has begun taking data at the Frascati φ-factory [3]. The experiment was designed to achieve an accuracy for the parameter $\Re(\varepsilon'/\varepsilon)$ of $\mathcal{O}(10^{-4})$. In order to achieve such final precision, the systematic uncertainty in the measurement of the branching ratios for $K_{L,S} \to \pi^+\pi^-$ and $\pi^0\pi^0$ must be kept below $\mathcal{O}(3 \times 10^{-4})$. This in turn requires that each contribution to the measurement uncertainty be kept well below 1×10^{-4}. The electromagnetic calorimeter and a large drift chamber are the two main components of the detector, see Fig. 1. The detector dimensions are driven by the mean decay length of K_L-mesons which at DAΦNE is 3.4 m. The detector dimensions indicated in Fig. 1 result in $\sim 30\%$ of the K_L-mesons decaying in a usable fiducial volume. Chamber and calorimeter are inside a super conductor coil which produces a field of 0.6 T. The primary functions of the calorimeter are the measurement of photon energies and position of entry. It also provides an accurate measurement of the time of arrival of particles.

Photons occur copiously in the decay of neutral pions, for example from $K_S K_L \to n\pi^0$'s as well as from many other reactions in φ-decays. The determination of the distance that K_L-mesons have travelled before decaying to π^0's is of crucial
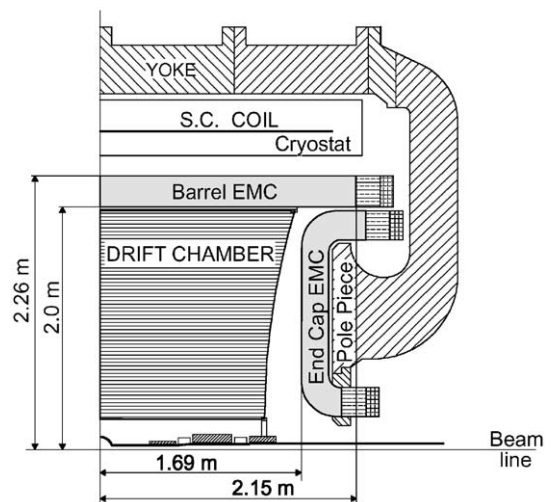

Fig. 1. Vertical cross-section of the KLOE detector, EMC stands for electromagnetic calorimeter.

importance in the study of CP violation. The travelled path is obtained from a measurement of the time of arrival of photons from π^0 decays. Since neutral kaons from ϕ-mesons decaying at rest travel with a velocity $\beta \sim 1/5$, time measurements with a precision of 100 ps allow to determine the flight path of a K_L decaying in $n\pi^0$ to ~ 0.6 cm, for a single detected photon. Such an accuracy is satisfactory for the KLOE aims, provided that the time scale is maintained to an accuracy of a few ps over the entire time of data collection which is of the order of 2–4 years.

The energy scale requirements are not particularly stringent, $\sim 5\%$ at the maximum energy of 1000 MeV. Again the energy calibration must be maintained to much higher accuracy, in average, over long times. This can be achieved with the KLOE detector by a continuous calibration of the relevant scales, simultaneous with data taking, utilizing a host of other processes, from Bhabha scattering events to many ϕ and kaon decay channels as stated in the original KLOE proposal, see Refs. [1,2]. Time and energy measurements, combined with momentum measurements with the drift chamber, also provide powerful means for charged particle identification.

This paper describes the KLOE electromagnetic calorimeter and is divided into two parts. The first part, Sections 2–7, describes the calorimeter structure, component selection, construction techniques, installation and electronics. Sections 8–13 deal with energy and time measurements, in particular the calibration procedures and the performance obtained with data from ϕ-decays.

2. Choices

An ideal electromagnetic calorimeter should provide the best resolution for measuring the energy and the entry point of photons. Special KLOE requirements are very good time resolution, full solid angle coverage and the smallest amount of dead material in front of the calorimeter. Finally, the energy range of interest is $20 < E < 510$ MeV. The above considerations have led to the choice of a lead-scintillating fiber sampling calorimeter. Scintillating fiber offers

several advantages, in particular they provide good light transmission over the required distances, up to ~ 4.3 m. Superior timing accuracy is obtained because of single mode propagation. Finally, it is easy to adapt the calorimeter shape to geometrical requirements, obtaining good hermeticity. No walls cover the active part of the calorimeter.

3. Calorimeter geometry

The almost cylindrical barrel (Fig. 1) consists of 24 modules; 4.3 m long, 23 cm thick and trapezoidal cross-section, with bases of 52 and 59 cm. Each end-cap consists of 32 vertical modules 0.7–3.9 m long and 23 cm thick. Their cross-section is rectangular, of variable width. Modules are bent at the upper and lower ends to allow insertion into the barrel calorimeter and also to place the phototube axes parallel to the magnetic field. Due to the large overlap of barrel and end-caps, the KLOE calorimeter has no inactive gap at the interface between those components. The central end-cap modules are vertically divided into two halves to allow the passage of the beam pipe and mounting in the detector the DAΦNE low-β insertion. Throughout this paper we use a coordinate system with z parallel to the beams, while x and y are horizontal and vertical, respectively, in a plane orthogonal to the beams.

All modules are stacks of some 200 grooved, 0.5 mm thick, lead foils alternating with 200 layers of cladded 1 mm diameter scintillating fibers, glued together with a special epoxy, which is not harmful to the fiber plastic. Fibers are mostly orthogonal to the entering particles in order to avoid channelling. This is particularly important at low energies [4]. In the final structure, fibers are at the vertices of an almost equilateral triangle of side 1.35 mm. The ratio, by volume, lead:fiber:epoxy is 42:48:10, the very high scintillator contents being necessary to obtain a good energy resolution. The average density is 5 g/cm^3, the radiation length is ~ 1.5 cm and the overall thickness of the calorimeter ~ 15 radiation lengths.

Read-out at both ends of each module is via light pipes which match almost square portions of the

module end faces to circular photo-cathodes. The read-out subdivides the calorimeter into five planes in depth, plane one through four, 4.4 cm deep. Plane five is 5.2 cm deep. Each plane is subdivided in the transverse direction into elements 4.4 cm wide, except at the edges of the trapezoidal modules. Five read-out segments aligned in ϕ for the barrel and in x for the end-caps form the almost projective towers, pointing toward the beam axis and toward a vertical line through the interaction point, IP, respectively. We refer to five such elements as a column. Columns are relevant to the calorimeter calibration procedures and in the trigger generation. The read-out segmentation gives an $r - \phi$ or $x - z$ read-out resolution of ~ 1.3 cm $(4.4/\sqrt{12})$, well matched to the shower size. A particle crossing the calorimeter deposits energy in at least five read-out regions or cells.

The calorimeter weight exceeds 100 tons and is viewed by 4880 photo-tubes.

4. Fiber selection and quality control

On the basis of tests [5], timing and energy requirements and cost considerations, we have chosen two types of fibers: Kuraray SCSF-81[3] and Pol.Hi.Tech. 0046 fibers.[4] The former have higher light output and longer attenuation length, while the latter are more economical. Our tests indicate that these kinds of fibers have attenuation length between 3 and 5 m and light yield equivalent to ~ 1 photo-electron/mm of crossed fiber at 2 m distance from a "standard" photo-tube. Moreover, the timing rms uncertainty of bundles of fibers is given by $\sigma_0/\sqrt{N_{pe}}$, where N_{pe} is the number of photoelectrons, and σ_0 is around 2.2–2.5 ns. σ_0 is the time spread for a single photoelectron and is dominated by the fast component of the scintillation decay time.

Fiber acceptance tests concentrated only on the relative measurement of attenuation length and light yield and were performed with a ^{90}Sr source moving along the fiber. The better fibers (Kuraray) are used in the inner half of the calorimeter

modules where most of the energy of photon showers is deposited. The total length of fibers used is 15,000 km.

Fluors and dyes are damaged by exposure to blue and near UV light. Kuraray fibers are particularly sensitive. A few days' exposure to daylight and industrial, i.e. mercury arc and similar light, severely reduces fiber quality [6]. Pol.Hi.Tech. fibers do not show similar losses of quality. Covering all windows with a standard yellow plastic film and use of incandescent filament lamps, in the modules' fabrication areas, eliminates the problem.

5. Module construction

Appropriate techniques and choice of components are important in the construction of the calorimeter stacks. One must ensure that no pressure is applied to the fibers to avoid damage to the cladding and the cladding core interface. Good timing requires that the light propagating in the cladding, which has more path length spread, does not reach the photo-tubes. The first point requires grooving the lead foils with indentations just barely larger than half the fiber dimension, the second is achieved by properly wetting the fiber surface with the epoxy mentioned above. This requires that the epoxy remains quite fluid for an appropriate time and that it is applied in very precise amounts to avoid irregular growth of the stack. Several tools were developed for rolling to shape the lead foil, for assembling the stack, controlling foil and fiber alignment, as well as uniform stack growth. At the end of the module assembly the resulting laminate is quite a rigid and sturdy material which can be reasonably handled and milled to final size. Construction of the end-cap modules requires 90° bending of the two ends. This step requires care but is in fact easy, if done before the epoxy is cured. Bending is done for a small number of layers at a time (10–15).

5.1. Construction tools

The grooved lead foils were fabricated by rolling 0.5 mm thick 95% Pb–5%Bi foils between two appropriately shaped rollers. The rollers were

---

[3] Manufactured by Kuraray, Japan.
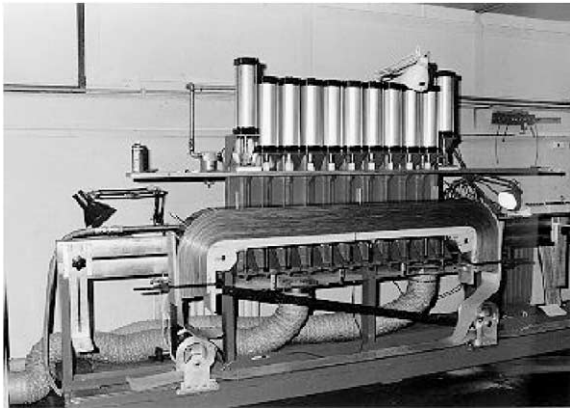[4] Manufactured by Pol.Hi.Tech., Italy.

Fig. 2. Assembly station for end-cap modules. In this picture a 3 m long end-cap module under construction is shown.

made of hardened steel ground to shape with diamond tools. Since the rollers were 60 cm wide, their alignment was critical. Additional pressure was applied in the middle of the grooving roller pair by a set of free wheeling rollers to control bowing. The results were excellent and the machine produced some 75,000 m, of up to 60 cm wide, grooved lead foil with only occasional realignment required. The rolling set was followed by cleaning and drying stations. Foil thickness was maintained within a few μm's and the grooves deviate from a straight line by less than 0.1 mm/m of foil length.

Assembly stations were built for the production of barrel and end-cap modules. One end-cap station is shown in Fig. 2 and is fully described in Ref. [7].

Vertical pistons, driven by high pressure gas, apply a pressure of about 1.1 atmospheres on the new stack of 10–15 layers, just after gluing and a stainless steel band holds in place the stack ends bent by 90° until the epoxy is cured. The station for assembly of the barrel module employs an evacuated rubber bag to pressurize the stack of area 0.6×4.3 m^2. Additional tools help in dispensing and positioning the fibers.

5.2. Construction procedure

The first lead foil is glued to a 25 mm thick aluminum back plate with a structural epoxy

which cures in ∼20 h. The three basic steps for building the stack are as follows:

(1) A precise amount of glue is spread over the lead foil.
(2) Fibers are laid down and, if necessary, manually fitted into the grooves. This is very easily accomplished by just passing a hand over the fibers.
(3) A new lead foil is laid down in place.

This last operation is critical because a mistake requires undoing one or more layers. The Bicron epoxy BC-600ML is mixed with a hardener/glue ratio of 0.28 for a pot life of 1.5 h, allowing the laying down up to 10–15 lead and fiber layers. During assembly, the stack was frequently checked, with machined rods and optically surveying equipment, for skewness of the layers to better than half a groove, over the full length, and uniform overall depth.

Precision sizing is obtained by milling end faces and sides of the cured module on a numerically controlled milling machine. The finished module is wrapped with 0.16 mm thick aluminum adhesive tape. This wrapping is the only dead material in the front and between modules.

5.3. Light guides

The light guides matching the module end faces to the photo-tube windows begin with a mixing section and terminate with a Winston cone [8] providing an area concentration factor of about 4. Since light propagates at small angles with respect to the fiber axis (∼22° for the light traveling in a plane containing the fiber axis), we expect to encounter very small light losses in the large area reduction. Measurements [9] show an overall efficiency for the guides we developed to be better than 80%, and a negligible degradation of the calorimeter performance. These losses are partly due to the interfaces introduced. Fig. 3 shows the light guides glued on one side of a barrel module. The light guides are positioned to an accuracy of better than 0.1 mm and glued on the module with the same Bicron epoxy mentioned. No wrapping is used, in order to avoid dead regions, resulting in a

Fig. 3. Light guides at one end of a barrel module before photo-tube installation.

Fig. 4. Exploded view of the PM box.

few % cross-talk between adjacent read-out elements which is of no consequence to the calorimeter performance.

5.4. Photomultipliers

To avoid mechanical complications (the magnet pole pieces open for detector maintenance) we chose to use photo-tubes capable of operating in magnetic field. Cavities in the pole pieces reduce the field to less than 0.2 T with a component transverse to the tube axis of less than 0.07 T. Structures with fine mesh dynodes and small drift space operate quite well under the above conditions, although some response and gain loss remain [10]. A disadvantage of this kind of structure is the low gain per stage and the partial loss in photo-electron collection, both resulting in larger signal fluctuation. We use Hamamatsu R5946/01 1.5' tubes. Gain and response of all photomultipliers have been measured before installation [11]. In the KLOE detector, the tube gains decrease by $\sim 10\%$ when the field is on, but linearity and resolution are not affected. The PMs are operated with grounded cathodes in order to eliminate leakages which can generate noise and field distortions in the PM. At the end of each module, a box holds the photo-tube mechanically in place and pressed against the light pipe ends, to which optical contact is made by means of Bicron optical gel BC-630. Inside the box there are cables
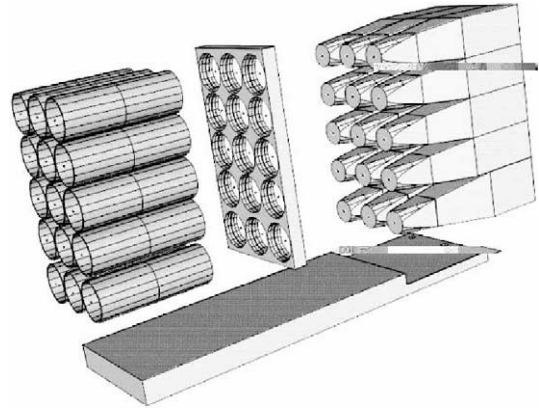
with connectors which are attach to the PM's bases. The cables carry high voltage, low voltage power, a test pulse and the output signal. An exploded view of the PM box, Fig. 4, shows the aluminum tubes containing the PMs with the high-voltage dividers and the preamplifiers and the plate through which tubes connect to light pipes. Tube caps spring load the PMs against the light guides.

6. Electronic read-out

A block diagram of the electronics for processing the photo-tube signals is shown in Figs. 5 and 6. The entire chain is AC coupled several times. While this results in a greater stability in static conditions, the effective zero offset for amplitudes and trigger thresholds becomes the function of data rates. Calculations show that, for appropriate choices of the time constants values of $\mathcal{O}(1 \text{ ms})$, the effect is negligible [12]. This is experimentally confirmed, see Section 11.1. The peculiar use of two capacitors and two $50 \, \Omega$ resistors in Fig. 5 allows us to achieve, ideally, a very large time constant for any value of the coupling capacitor.

6.1. The preamplifier

The PM signal is coupled to a 12 m long, $50 \, \Omega$, miniature coaxial cable terminated at both ends
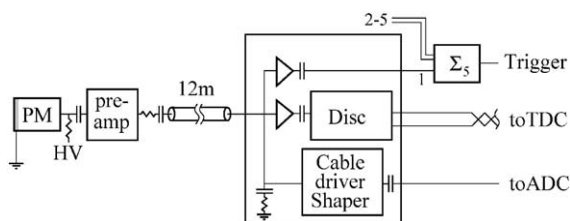
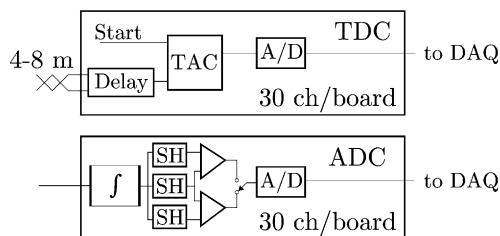Fig. 5. Block diagram of preamplifier and auxiliary circuits.

Fig. 6. Block diagram of ADC and TDC.

through an AC coupled preamplifier. Use of a preamplifier allows a better coupling to the cable but, more importantly, to operate the tubes at lower anode pulse current.

The divider current can correspondingly be lower, decreasing power dissipation in the tube boxes and extinguishing the tube. This avoids the possibility of excessive dissipation on the anode, therefore guaranteeing long tube life. Total dissipation of divider plus preamplifier is about 60 mW/channel.

The entire electronics following the preamplifiers has a modularity of 30 channels, or 6×5 columns, to simplify cabling and maintaining readout proximity for trigger purposes.

6.2. The driver–adder–discriminator board

After 12 m of cable, the signal is split into three ways: a discriminator, a driver and an adder. The stop signal for the TDC is produced by a constant fraction discriminator with low time walk. The output, a differential current signal to avoid problems from poor connector contacts, is sent by a twisted pair to the TDC. The effective

thresholds are in the range 4–5 mV. They correspond to signals originated by 3–4 photoelectrons or energy deposits of a 3–4 MeV photon at 2 m from the photomultipliers. 30 channels of the above are housed on a 9U VME board called an SDS board and 16 boards are in a crate. The VME busses are not used. Boards communicate via a crate controller with the KLOE slow control system, for thresholds downloading and temperature or supply voltages monitoring.

6.3. ADC and TDC boards

Processing of the detector signals poses special problems because the particle arrival times for an event have spreads of up to 250 ns. Furthermore, due to the cable configuration, signals at the input of the ADC (TDC) can precede the trigger by as much as 350 (220) ns. KLOE solutions are sketched in Fig. 6 and described in the following.

A 12 bit ADC [13] for energy measurements, with an effective sensitivity of ~ 5 count/MeV of energy deposition in the calorimeter was developed, partly in collaboration with industry.[5]

Arrival time problems are avoided by sampling techniques. Two sample and hold (SH) devices alternatively acquire the signal at the output of an integrator whose decay time is 5 ms. The acquisition interval is 600 ns and the two channels run $180°$ out of phase. Upon receipt of a trigger, a third channel acquires, after appropriate delay, the integrator signal which equals the baseline value plus the signal of interest. The correct value is recovered by subtracting the signal stored in the appropriate SH channel. The ADC contributes a total rms noise lower than 1 count. Integral nonlinearity is better than 0.3% of full scale. The ADC has a zero offset of ~ 250 counts with a spread of $\pm 3\%$. The conversion gain has a similar spread.

A 12 bit TDC [13] with a sensitivity of 53 ps/count and a range of 220 ns was designed for time measurements. The TDCs work in common start mode. The stop signals are delayed by 220 ns with a mono-stable to accommodate the trigger formation time. The TDC is built around a
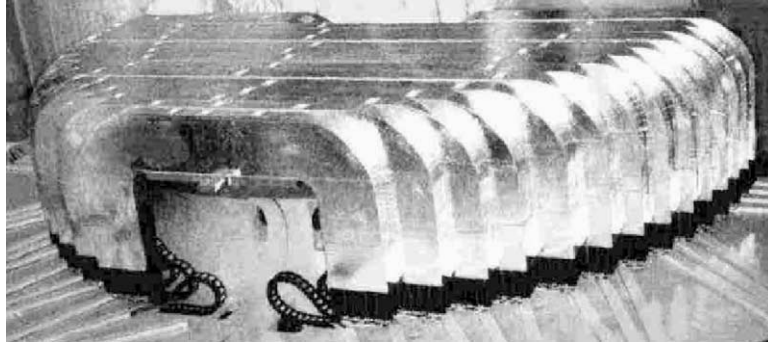
---

[5] CAEN, Viareggio, Italy.

Fig. 7. Half of one end-cap, mounted on the yoke pole piece. The picture is shown rotated form vertical to horizontal.

monolithic time to analog ramp converter. Resolution is better than 1 count, integral non-linearity is better than 0.2% of full scale. The temperature coefficient is compensated to be smaller than ± 60 ppm/$^{\circ}$C.

ADCs and TDCs are implemented on $9U \times 400$ mm VME boards with full VME interface to a 32 bit bus. Each board houses 30 ADC or TDC channels, implements empty channel flagging and suppression and has a custom interface for sparse data scan read-out via an additional bus, called auxbus, and a crate read-out controller, ROCK, both developed by the KLOE collaboration [14].

7. Calorimeter installation

Barrel modules are attached to the inner wall of the coil cryostat. A system of rails, cams and screws allows the insertion and positioning of each module to a final accuracy of better than 1 mm. Modules are brought to the proper height and orientation before insertion with a lifting table loaned by CERN.[6] A rotating cage for orienting each module to the appropriate azimuth, was installed on the table.

End-cap modules are first assembled as the two halves of each end-cap, in a horizontal position. They are then raised to a vertical position and lifted in place with a crane. The separation of the
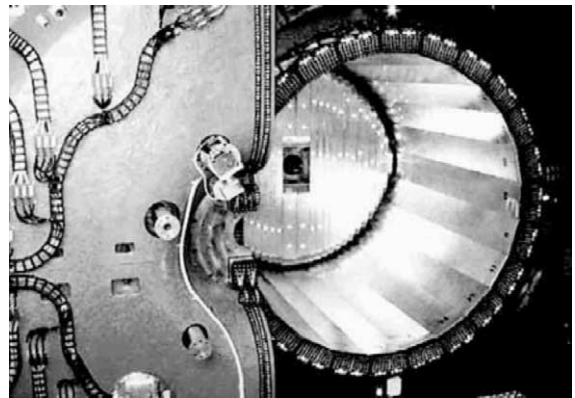
Fig. 8. A view of the complete KLOE calorimeter. The far end-cap is closed. The near yoke pole piece and end-cap calorimeter are open.

end-caps into two halves allows the opening for access to the chamber. One of these halves is shown in Fig. 7.

Each half end-cap is mounted on a 3 cm thick iron plate, which in operation is flush against the pole piece faces. Each half end-cap assembly is hung from motor driven iron pistons penetrating through the yoke which allows separating them from the yoke for access to the photo-tubes hidden in the mentioned cavities. Fig. 8 shows barrel and end-caps after the installation, before insertion of the drift chamber. A final survey of the whole calorimeter provides the positions of each module with an accuracy of the order of 0.1 mm.

---

[6] We thank B. Bloch of Saclay.

8. Reconstruction of time, position and energy in a calorimeter cell

The calorimeter read-out granularity is defined by the light collection segmentation. The fiber's direction is referred to in the following as longitudinal. This segmentation provides the determination of the position of energy deposits in $r - \phi$ for the barrel and in $x - z$ for the end-cap. A calorimeter segment is called in the following a cell and its two ends are labelled as A and B. For each cell, two time signals, $t^{A,B}$ and two amplitude signals $S^{A,B}$ are recorded from the corresponding PM's signals. The longitudinal position of the energy deposit is obtained from the difference $t^A - t^B$.

The particle arrival time t and its coordinate s along the fiber direction, the zero being taken at the fiber center, are obtained from the times $T^{A,B}$ in TDC counts as

$$t \ (\text{ns}) = \frac{t^A + t^B}{2} - \frac{t_0^A + t_0^B}{2} - \frac{L}{2v}$$

$$s \ (\text{cm}) = \frac{v}{2}(t^A - t^B - t_0^A + t_0^B)$$

with

$$t^{A,B} = c^{A,B} \times T^{A,B}$$

where $c^{A,B}$ (in ns/TDC counts) are the TDC calibration constants and $t_0^{A,B}$ are the overall time offsets. L and v are the cell length (cm) and the light velocity in the fibers (cm/ns), respectively. The energy signal, E, on each side of a cell i is obtained from S as

$$E_i^{A,B} \ (\text{MeV}) = \frac{S_i^{A,B} - S_{0,i}^{A,B}}{S_{M,i}} \times \kappa_E. \tag{1}$$

All signals S above are in ADC counts. $S_{0,i}$ are the zero-offsets of the amplitude scale. $S_{M,i}$ is the response for a minimum ionizing particle crossing the calorimeter center. Dividing by $S_{M,i}$, Eq. (1) above, accounts for PM response, fiber light yield and electronics gain. κ_E gives the energy scale in MeV, and it is obtained from showering particles of known energy.

In order to obtain a calorimeter response independent of the position, a correction factor $A_i^{A,B}(s)$, due to the attenuation along the fiber length, is applied. The cell energy, E_i, is taken as the mean of the determinations at both ends.

$$E_i \ (\text{MeV}) = (E_i^A A_i^A + E_i^B A_i^B)/2.$$

9. Calorimeter performances early tests

9.1. Beam tests

Before starting the production assembly of the modules, several calorimeter prototypes were studied. A prototype full size barrel module was tested in June 1994 at PSI [15,16]. The module was assembled with its final PMs and read-out by a prototype version of ADC and TDC boards. An energy resolution of $5\%/\sqrt{E \ (\text{GeV})}$ for electrons in the energy range 50–300 MeV was found in agreement with previous measurements. The measured time resolution of $70 \ \text{ps}/\sqrt{E(\text{GeV})}$ was worse than expected, due to the lower quality of the fibers used for the prototype module.

9.2. The cosmic ray test stand

A cosmic ray test stand (CRTS) was built and operated at the Frascati Laboratories during the assembly and the construction of the calorimeter modules [17,18]. Four layers of streamer tubes and 12 scintillator counters allowed the reconstruction of the trajectory of cosmic ray particles in the calorimeter modules with a precision of $\sim 1 \ \text{cm}$ while providing a trigger. Up to four modules were tested simultaneously. All modules were tested at the CRTS with their final PMs. The purpose of the test was two-fold:

- Verify that all cell of the modules are up to specifications in terms of photo electron yield and attenuation length.
- Determine the first high voltage value for each PM, equalizing the response for minimum ionizing particles crossing at the module center.[7]

---

[7] The responses are equalized in terms of integrated charge per unit path length. Since the minimum ionizing particles path in the 5th plane cells is larger by a factor 1.18 with respect to all the other cells, these cells are equalized to a larger value.

Since long modules are built with better fibers and have higher quantum efficiency photubes, the overall spread in high voltage settings is reduced. The voltage values for equal response in signal per unit energy deposit is obtained by iteration. We use the empirical relation $S \propto V^7$, approximately valid for the tubes employed.

We notice that equalization of channel responses is not necessary for determining shower energies, since accurate calibration constants are used. However, the calorimeter signals are employed to generate a trigger, after several levels of signal additions. The trigger requires a response equalization to a few %.

10. Electromagnetic shower reconstruction

The measurement of energy, position and arrival time requires the recognition of which signals belong to a particle entering the calorimeter. This operation is performed by a *clustering algorithm*. The first step groups cells, contiguous in $r - \phi$ or $x - z$, into pre-clusters. In the second step, the longitudinal coordinates and the arrival times are used for further merging and/or splitting of the preclusters.

Cells are included in the cluster search only if times and amplitudes are available from both
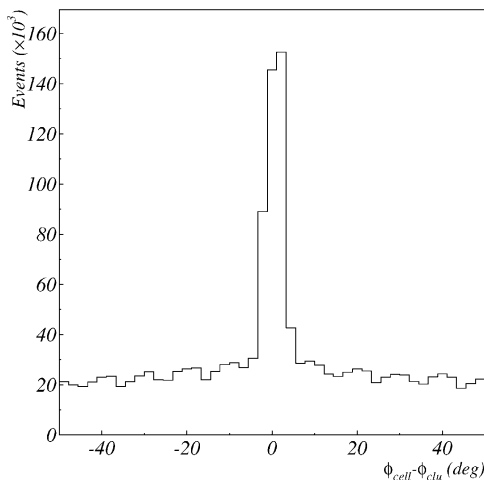
Fig. 9. Distribution of $\Delta\phi = \phi_{\text{cell}} - \phi_{\text{cl}}$ for barrel "incomplete" cells. The strong correlation defines a clear "recovery" region.

sides. If a cell is missing time and/or amplitude signals, it is called an "incomplete" cell. For the barrel calorimeter, "incomplete" cells are recovered on the basis of the difference $\Delta\phi$ between its azimuth and that of the closest cluster. The distribution of $\Delta\phi$ for a sample of Bhabha events, Fig. 9, shows a clear correlation. Incomplete cells are assigned to the cluster if $|\Delta\phi| < 3°$. A similar procedure is used for the end-caps using the transverse coordinate x. The cluster energy, E_{cl}, is the sum of the energy of all cells assigned to a cluster. The cluster position, $\{x, y, z\}_{\text{cl}}$, and the cluster time, T_{cl}, are computed as energy weighted averages of the cells' variables.

11. Energy measurements

In this section, the determination of the zero-offsets is described together with the energy calibration procedure using minimum ionizing particles and electromagnetic showers. The results on linearity in energy response, energy resolution and mass reconstruction are also presented.

11.1. Zero-offset determination

During data taking, empty channel read-out suppression, defined below, is necessary. Energy zero-offsets are obtained from cosmic ray runs without circulating beams, i.e. with very low occupancy of the detector. The energy scale offsets S_0 and their rms fluctuations σ_{S_0} are computed from the collected data. Pulser triggered runs are also used for comparison showing no relevant differences. To check the effect of high signal rate on the zero-offsets, runs with beams colliding and without empty channel suppression have been studied, showing no relevant effect. Channel read-out is suppressed if $|S - S_0| < 3\sigma_{S_0}$. Most of the offset rms fluctuations are below 4 ADC counts or less than 1 MeV energy deposit. The *noisy* channels, with $\sigma_{S_0} > 20$ counts, are in a number of about 10 out of a total of 4880. Long term drifts are below 1–2 counts per month, Fig. 10. Since zero-offset calibration requires only few minutes, it is performed daily.
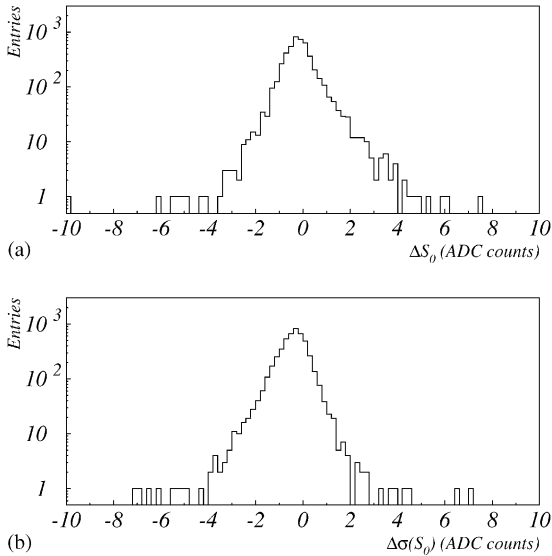
Fig. 10. Amplitude zero-offset stability. (a) Offset differences for two runs one month apart. (b) Offset rms fluctuation.

11.2. Energy calibrations using minimum ionizing particles

A relative energy calibration of all calorimeter cells is obtained with cosmic ray minimum ionizing particles. The same data determines the response dependence on position along the fibers. From the 2.5 kHz cosmic ray trigger, 50–100 Hz of high quality minimum ionizing particles crossing the calorimeter, are selected on-line. The requirement that the first and the last cells of the same column are traversed, reduces by a factor of ~ 10 the azimuthal rate dependence. Particles are further required, off-line, to cross one column only and to be almost orthogonal (within $10°$) to the calorimeter surface. Due to the dependence of the cosmic ray flux with respect to the vertical direction, the last requirement results in different angular distributions of the samples selected in the barrel and in the end-cap. This in turn corresponds to different path lengths in the two subdetectors.

During a typical cosmic ray run, about 18 h of data taking, ~ 1000 events at the center of each cell are collected. An amplitude spectrum is shown

in Fig. 11. The distribution is, as expected, skewed toward high energy losses. A fit is performed to a region centered at the most probable value and $\pm 2\sigma$ wide. The peak of the distribution defines S_M. The statistical uncertainty of the determination is 1–2% (see Fig. 12a). Reproducibility between two consecutive calibrations is shown in Fig. 12b).
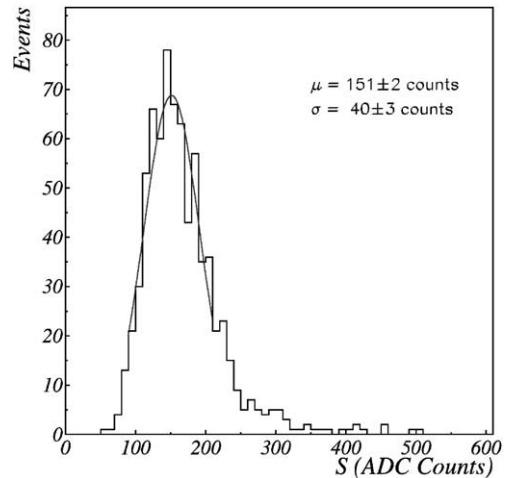
Fig. 11. Energy signal spectrum for minimum ionizing particles. Only a limited region around the peak is fitted.
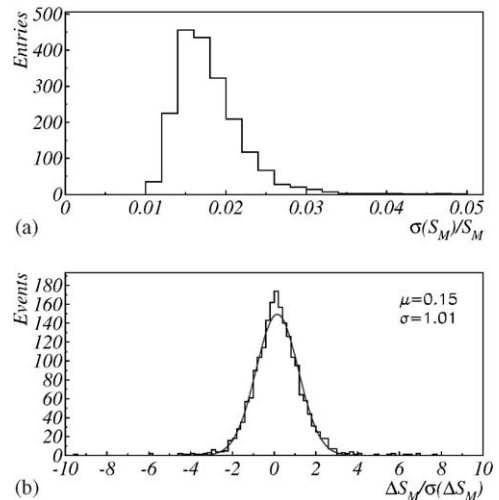
Fig. 12. (a) Distribution for all barrel channels of $\sigma(S_M)/S_M$. (b) Distribution of the difference $\Delta S_M / \sigma(\Delta S_M)$ between two calibrations.

$\lambda_1 = 37 \pm 4$ cm

$\lambda_2 = 470 \pm 10$ cm

$A = 0.27 \pm 0.01$
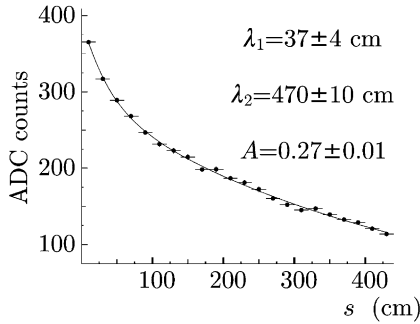
Fig. 13. Signal from minimum ionizing particles vs. s. λ_1 and λ_2 are the two attenuation lengths and A the relative weight of the two exponential components.
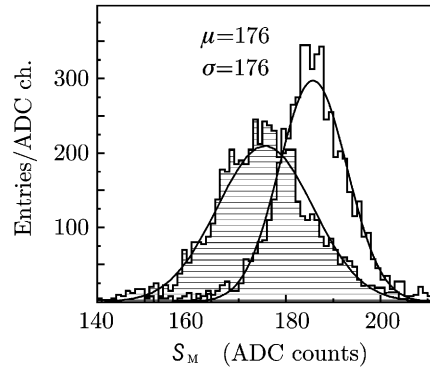

$\mu = 176$
$\sigma = 176$

Fig. 14. Effect of the magnetic field on calorimeter response for the four innermost planes of barrel. Solid (hatched) histograms are without (with) magnetic field on. The μ and σ values are the mean and the rms spread with magnetic field on.

The dependence of the ADC output S on the distance s from the module end is shown in Fig. 13 for one barrel channel. The data are fitted with the sum of two exponentials. The "long" component is ~ 500 cm, in agreement with the previous measurements [18].

11.3. Magnetic field effects

Fig. 14 shows an example of the distributions of the S_M values determined, without and with magnetic field, for the four innermost planes of the barrel calorimeter. Similar results are obtained for the entire calorimeter. In the barrel, the main effect is a lowering of the photo-tube output signal by 5%. The broadening of the distribution is due to the fact that the data were taken with the high voltage settings optimized for the case of field off. Since each photo-tube observes a different magnetic field, a broadening of the gain's distribution is to be expected.

The increase of the width is larger for end-cap channels where larger field variations are present. Equalization of all channels to better than 5% is obtained with a gain-equalization procedure similar to the one described in Section 9.

The result is shown in Fig. 15. Minimum ionizing particles generate signals of different average heights in barrel and end-caps, because the path length of the cosmic ray particles is different in the two detectors.

(a) $\sigma/\text{peak} = 3.0\,\%$

(b) $\sigma/\text{peak} = 5.4\,\%$

Fig. 15. Distribution of the minimum ionizing particle signal for all calorimeter channels of the barrel (a) and end-cap (b).

11.4. Stability of calibration with minimum ionizing particles

Figs. 16(a) and (b) show the change in calorimeter response over an interval of two months without changes in high voltage. While the mean values have not changed, a broadening of the widths by $\times 1.8$ indicates that individual channel gains have drifted by about 2–4%. The overall mean drift over most of 1999 in Fig. 16(c) shows
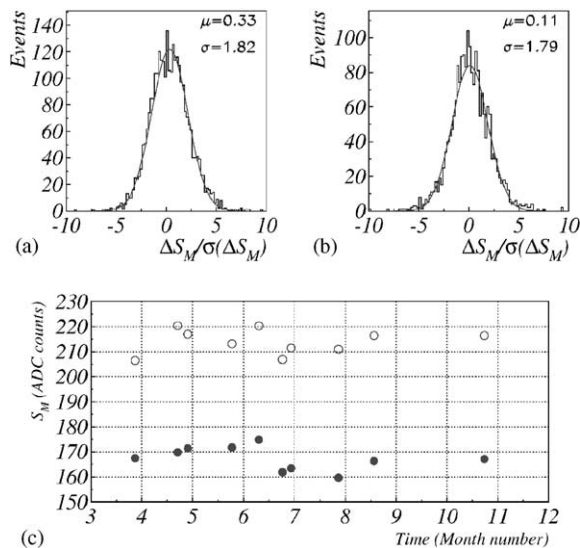
Fig. 16. Calibration stability. $\Delta S_M/\sigma(\Delta S_M)$ distributions for barrel (a) and end-cap (b) over a two month interval. Average value of S_M (c) during 1999.

overall long term response variations below 5%. These response changes do not affect the trigger. The energy measurement accuracy is however maintained since the correct calibration constants are used in reconstruction.

11.5. Calibration using e.m. showers

The absolute energy scale factor κ_E, see Eq. (1), is best determined from data, with an ultimate accuracy given by the knowledge of the φ-meson mass, $m(\phi) = 1019.417 \pm 0.014$.

Samples of Bhabha and 2γ events, selected on-line, are used to perform this final calibration. An integrated luminosity[8] of 100 nb^{-1} yields 40,000 Bhabha and 5000 2γ events in the barrel and 120,000 Bhabha and 4000 2γ events in the end-caps. Bhabha and 2γ events are easily separated since the two clusters are not collinear with the interaction point for Bhabha's due to the bending in the field, see Fig. 17. Bhabha events are more abundant and are used to determine the relative cell response while 2γ events suffer less energy losses and are better for setting the energy scale.

----

[8] Roughly 1 day of data collection during December 1999.

Fig. 18 shows the cluster energy, E_{cl}, vs. azimuth for Bhabha events before and after an iterative calibration procedure. The same procedure is employed for the end-caps. The energy scale is set imposing $M_\phi/2$ on the peak of the photon energy distribution for e$^+$e$^- \to 2\gamma$ events. The κ_E factor found is ~ 40 MeV/S_M. Since at the CRTS, an average number/side of 35 photoelectrons/minimum ionizing particle at the calorimeter center was measured [17], it results in a light yield of about 1 p.e. per MeV deposit at the calorimeter center.
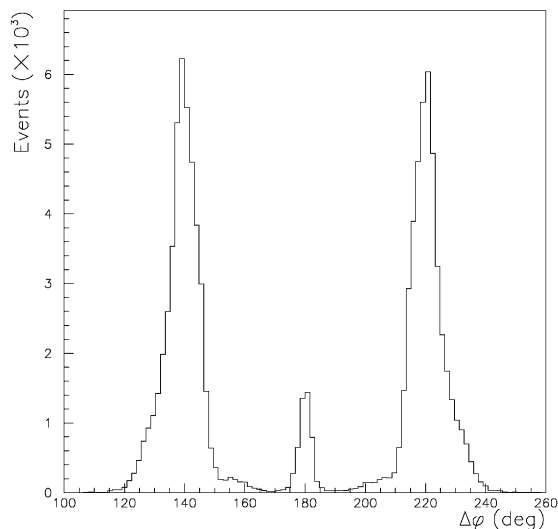
Fig. 17. Azimuth distributions of the two energy clusters for Bhabha and 2γ events. The peak at $\Delta\phi = 180°$ is due to γγ events, while the others are due to Bhabha events.
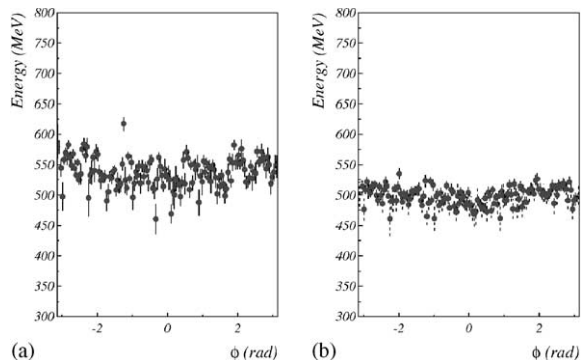

Fig. 18. Distribution of E_{cl} vs. φ for Bhabha events in the barrel. (a) Before the calibration procedure. (b) After.

The absolute energy scale fluctuates by less than 5% during a 6 month period. Such variations are corrected by frequent recalibration.

11.6. Boundary region effects

Although the detector covers $\sim 98\%$ of 4π, the regions between columns and at the module edges deserve closer attention in determining the actual energy response. Fig. 19 shows the distributions E_{cl} vs. azimuth in the barrel and vs. x in the two end-caps for Bhabha events. No cross-talk or signal loss is detectable at light guide boundaries. Losses of up to 10% are instead evident between modules. A correction for this effect must be applied at analysis level.

11.7. Energy resolution and energy response

Energy resolution and linearity of the calorimeter, are obtained using photons covering the full energy spectrum. Radiative Bhabha events provide γ's covering a wide energy and angular range. Event reconstruction from tracking information determines the γ direction and energy, E_γ, with good accuracy. A match between the above γ direction and the cluster position is required. For each 10 MeV energy interval in E_γ, the distribution of $E_{cl} - E_\gamma$ is fitted with a Gaussian to find its central value. Fig. 20(a), shows $(E_{cl} - E_\gamma)/E_\gamma$ vs. E_γ. Linearity is better than 1% for $E_\gamma > 75$ MeV. Deviations from linearity at the 4–5% level are observed below 75 MeV probably due to both the low energy cutoff introduced by the ADC thresholds and to the loss of shower fragments. The energy resolution as a function of E_γ is shown in Fig. 20(b). By fitting the resolution with the usual $a/\sqrt{E(\text{GeV})} + b$ parameterization, one obtains $a = 5.7\%$, while the constant term b is negligible. The resolution is dominated by sampling fluctuations with contributions from photoelectron statistics.

11.8. Neutral particles masses: π^0, η and K_S

A large sample of $\phi \to \pi^+\pi^-\pi^0$ decays has been used for the π^0 mass and radiative decays $\phi \to \eta\gamma$ for the η mass. The $\pi^+\pi^-\pi^0$ events are identified
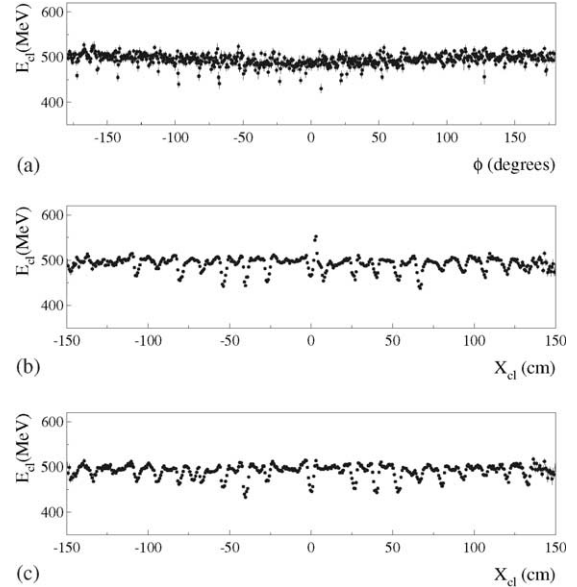

Fig. 19. Bhabha calorimeter response vs. azimuth in the barrel (a) and along the horizontal coordinate x in the two end-caps (b and c).
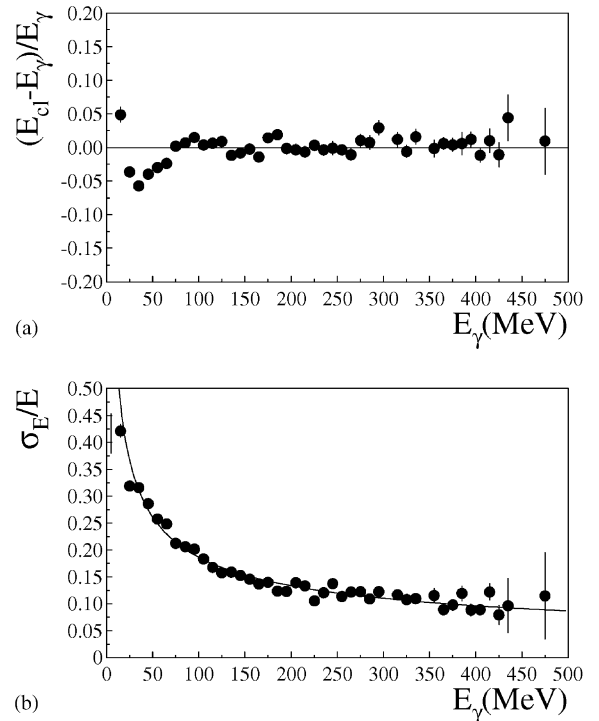

Fig. 20. $(E_{cl} - E_\gamma)/E_\gamma$ (a) and resolution (b) vs. E_γ for $e^+e^-\gamma$ events. The fit gives $\sigma(E)/E = 5.7\%/\sqrt{E(\text{GeV})}$.
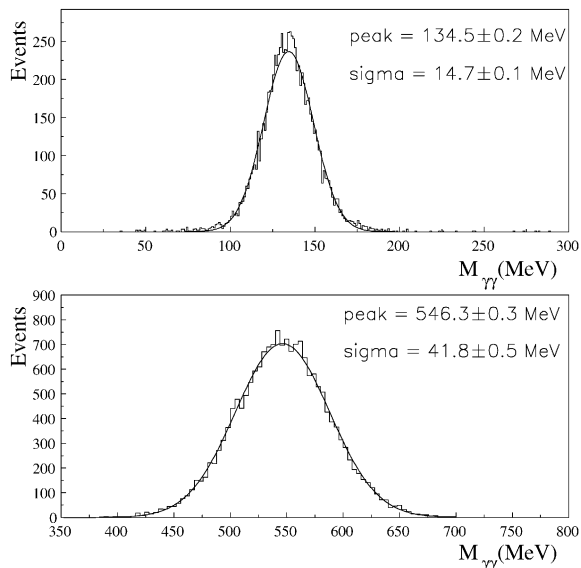
Fig. 21. Invariant mass distribution of photon pairs from $\pi^+\pi^-\pi^0$ events with $\pi^0 \to \gamma\gamma$ events (top) and from $\eta\gamma$ with $\eta \to \gamma\gamma$ events (bottom).
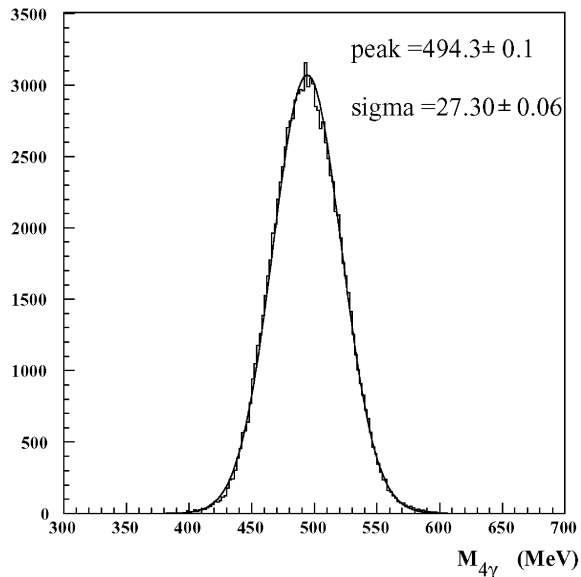

Fig. 22. K_S mass from photon energies in $K_S \to \pi^0\pi^0$ events.

by two tracks from the interaction point, plus two calorimeter clusters not associated with tracks. The reconstructed $M(\pi^0)$ is shown in Fig. 21. The value is correct within 0.6% [19] $\eta \to \gamma\gamma$ events are

from a sample of radiative ϕ-decays [20]. Fig. 21 also shows the η mass peak, with a value correct to better than 0.4%.

A clean sample with four photons in the final state is provided by $K_S \to \pi^0\pi^0$ decays. Due to the short lifetime of the K_S, $\langle L(K_S) \rangle \sim 6$ mm, we use the interaction point as the decay vertex. Fig. 22 shows the K_S mass peak from ~ 2 pb^{-1} of data. Agreement with the known mass is better than 1%.

12. Time measurements

Determination of t, see Section 8, is more complicated because knowledge of the collision time is necessary in addition to the light velocity in the fibers v, the time offsets $t_0^{A,B}$, the cell lengths (L) and the TDC scale factors, $c^{A,B}$. At DAΦNE, there is in average one collision per 10^6 bunch crossing. The trigger cannot be used as the time scale origin because of the large spread of arrival times. Thus, the interaction time must be found event by event from the data. To help in the accuracy of the collision time determination, the fast trigger signal is synchronized with a clock, T_{clk} in the following, phase locked with the DAΦNE radio frequency. The T_{clk} period is a multiple of the RF period, $T_{RF} = 2.715$ ns. The interaction time thus needs to be determined only to an accuracy of ~ 2 ns, in order to choose between neighboring bunch crossings.

The scale factors for all TDCs were measured prior to installation. On an average, $c \sim 53$ ps/count with an uncertainty of $\leqslant 0.3\%$. The lengths of every cell have been measured by survey, prior to installation. The values of v and $t_0^{A,B}$ are obtained as described below. Pulse signals injected in the preamplifiers allow the measurement of time offsets due to the cable lengths, the delay provided by the TDC mono-stable and so on, only to ~ 1.5 ns. Better values of v and corrections to the time offsets are obtained with cosmic ray data. The final corrections to the $t_0^{A,B}$ values are obtained using $e^+e^- \to \gamma\gamma$ events.

This calibration procedure is repeated periodically and the resulting calibration constants are entered in a database. The calorimeter reconstruc-

tion program reads the database according to run number.

12.1. Timing calibration with cosmic rays

The values of v and of the time offsets are obtained with cosmic rays data, collected with or without beams circulating in DAΦNE. For each cell, the $t^A - t^B$ distribution, see Fig. 23, determines $t_0^A - t_0^B$ and v, given, respectively, by the center and the width of the spectrum. Iterations are performed minimizing the time residuals of the reconstructed cosmic ray tracks. This procedure is best for straight tracks. We, therefore, require $p > 7$ GeV/c from tracking in the chamber. Fig. 24 shows the distribution of the residuals for increasing iteration cycles. The single side time offsets are obtained by combining the evaluated t_0 sums and differences. With a 10^6 events run, about 10 min, these offsets are evaluated with a statistical uncertainty between 50 and 80 ps depending on the illumination of the cell.

Charged tracks reconstructed by the chamber provide the entry position s_{DC} along the calorimeter cell. The values of $t_0^A - t_0^B$ and v obtained from calorimeter information can thus be checked.

Fig. 24. t_0 correction during iteration for all calorimeter channels. Few iterations are sufficient.
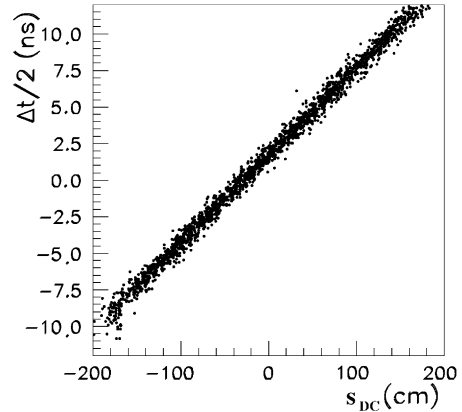
Fig. 25. $(t^A - t^B)/2$ vs. s_{DC} for a barrel cell.

$t^A - t^B$ vs. s_{DC} is a straight line with a slope given by $2/v$ and intercept $t_0^A - t_0^B$. An example is shown in Fig. 25. A good agreement is observed by comparing v and $t^A - t^B$ measurement with the two methods.

12.2. Calibration using $e^+ e^- \to 2\gamma$ events

12.2.1. Determination of the global time offset $t_{0,G}$

The DAΦNE radio frequency has a period $T_{RF} \sim 2.71$ ns and the interval between two

Fig. 23. $t^A - t^B$ spectra. The center of the distributions give $t_0^A - t_0^B$. The light velocity v is obtained from the width.

consecutive bunch crossings is $n \times T_{RF}$ with $n = 1$–4, typically. During 1999, n was 2. As mentioned earlier, the correct collision time must be obtained from the event data.

The time of flight of photons for $e^+e^- \rightarrow 2\gamma$ events is r_{cl}/c, with r_{cl} the distance of the cluster from the interaction point. The distribution of the difference, $t_{res} = t_{cl} - r_{cl}/c$, between measured and expected time of flight, Fig. 26, shows well separated peaks due to the spread in trigger time after synchronization with the T_{clk} signal. The distance between peaks gives an estimate of T_{RF}, called here $t_{RF}^{2\gamma}$. In principle, any peak can be chosen as reference time. Arbitrarily, the time of the peak in the $(48, 51)$ ns window is used as reference time $t_0^{2\gamma}$.

Long term drifts of $t_0^{2\gamma}$ and of $t_{RF}^{2\gamma}$ are shown in Fig. 27. Fluctuations of $t_0^{2\gamma}$ of $\mathcal{O}(100\ ps)$ are due to the T_{clk} phase with respect to the bunch crossing which changes with run conditions. $t_0^{2\gamma}$ and $t_{RF}^{2\gamma}$ are used to determine the global time t_0^G of each event as $t_0^G = t_0^{2\gamma} + k t_{RF}^{2\gamma}$. For each event, the integer k is found, determining unambiguously the correct beam crossing.
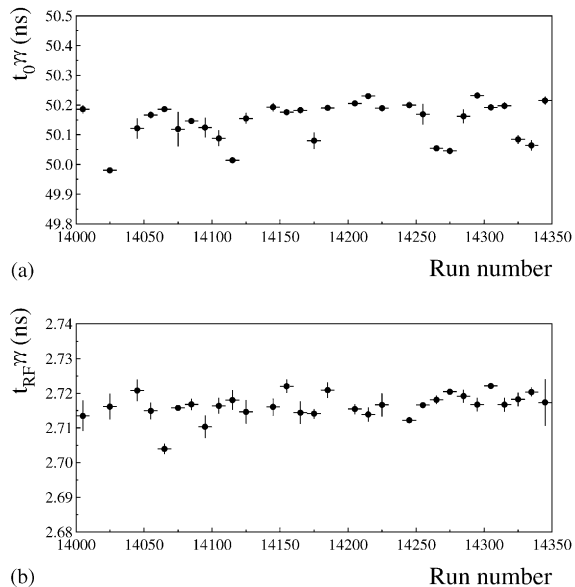

Fig. 27. $t_0^{2\gamma}$ (a) and $t_{RF}^{2\gamma}$ (b) vs. run number for one month of data taking.

12.2.2. Corrections to the TDC calibration constants

The TDC constants $c^{A,B}$ originally measured in a laboratory test stand, are good up to an overall scale factor. An absolute calibration can be obtained using the DAΦNE RF signal. The ratio $t_{RF}^{2\gamma}/T_{RF}$ gives, in fact, the TDC scale correction. This correction, ~ 1.01, is the same for all channels. A 0.5% error on the time scale corresponds to an error of 30 ps for the time of flight of a prompt photon and of 150–200 ps for the time of flight of a K_L reaching the calorimeter.

12.2.3. Fine relative time offset corrections

The 2γ events are used to find the fine corrections to the time offset determined and obtained with cosmic rays. The correction is presently at the column level because of statistics but is, anyway, the most relevant one. Comparing the column T_{res} for a cluster, the residual spreads are minimized by an iterative procedure. Fig. 28 shows the $t_0^{A,B}$ values before and after three iterations. The accuracy of the method is of $\mathcal{O}(20\ ps)$ for 100 nb^{-1} of collected data.

Fig. 26. $t_{cl} - r_{cl}/c$ distribution for 2γ events. Peaks are separated by T_{RF}.
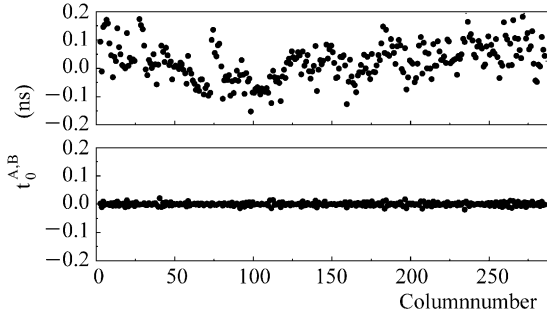
Fig. 28. Corrections to the time offsets vs. column number before and after three iterations. The initial spread is after the cosmic ray calibration.

12.3. Timing resolution of the calorimeter

The timing accuracy of the calorimeter has been determined with cosmic rays, 2γ, radiative Bhabha and ϕ radiative decay events. In this section we present results from the above processes and also a study of K_L decays and K_L interactions in the calorimeter.

12.3.1. Timing with cosmic rays

The analysis described in Section 12.1 gives, for each cell, the width of residual distributions, which is approximately the time resolution of a cell for an energy deposit equivalent to a ~ 40 MeV photon. Fig. 29 shows an example, before and after applying the corrections. The resolution is 260 ps, in agreement with a scaling law of ~ 54 ps$/\sqrt{E(\text{GeV})}$ considering a 40 MeV equivalent energy release.

The resolution in the coordinate s is obtained by comparing the coordinates reconstructed by the calorimeter with those obtained from tracking, Fig. 30. The cell resolution is of the order of 5 cm in agreement with the quoted time resolution.

To check the performance of the calorimeter as a time of flight detector, we select cosmic ray events with two opposite clusters connected by a single track in the drift chamber. For such events the drift chamber information provides the track length L_{tr} and the momentum p of the track. In Fig. 31, the cosmic ray velocity given by $\beta_c = L_{\text{tr}}/|t_{\text{cl}}^1 - t_{\text{cl}}^2|$ is plotted as a function of the track momentum p. The data are fitted with β vs. p relation $\beta = p/\sqrt{p^2 + m^2}$ where m, the mass of the
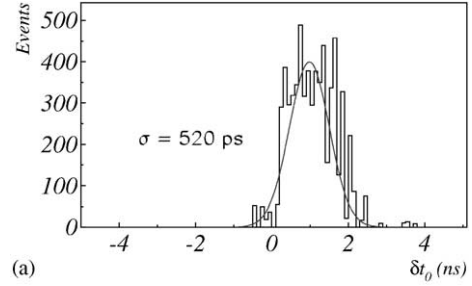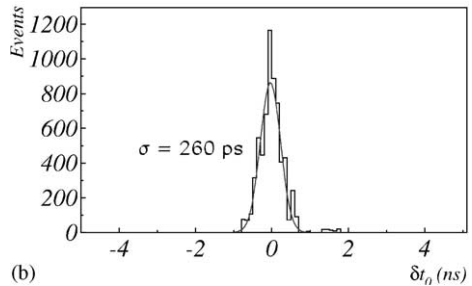
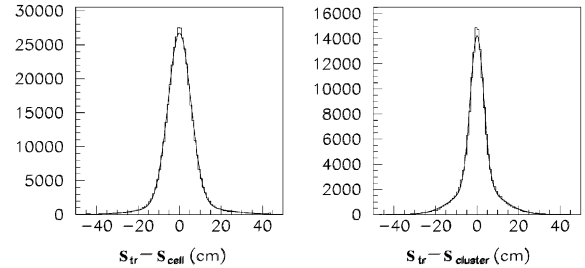Fig. 29. Residual distributions before and after t_0 corrections using cosmic ray particles.

Fig. 30. A comparison of tracking and calorimeter determination of the coordinate s along the fiber. s_{tr} is obtained from tracking. s_{cell} for single cells and s_{cl} for clusters are the values found with the calorimeter.

particle, is the only free parameter. The value of m obtained by the data is compatible with the muon mass, as expected.

12.3.2. Time resolution with photons

The timing resolution is given in Fig. 32 for photons from radiative ϕ decays as a function of E_γ. Good agreement between the different measurements is observed down to 100 MeV. The curve in the plot is a fit yielding

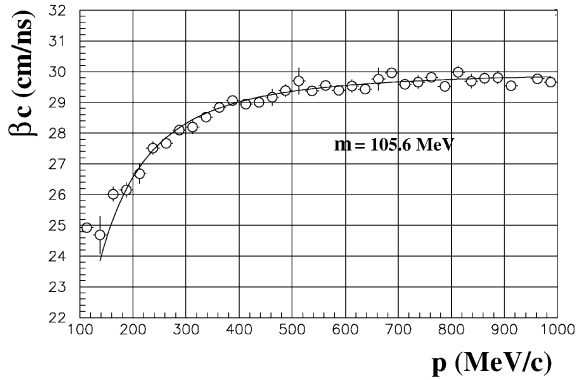$$\sigma_t = 54 \text{ ps}/\sqrt{E(\text{GeV})} \oplus 140 \text{ ps}$$

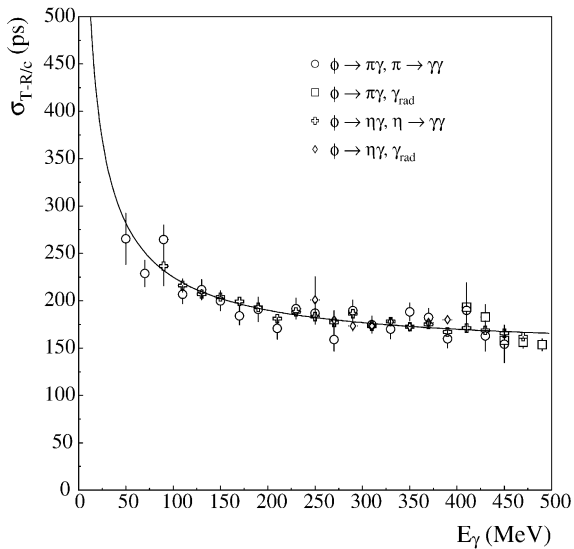Fig. 31. Velocity as a function of track momentum for cosmic ray events.

Fig. 32. Time resolution as a function of E_γ for ϕ radiative decays.

where the sampling fluctuation term is in agreement with test beam data, and the second term is a constant to be added in quadrature. The constant term is due partly to residual calorimeter miscalibrations, but mostly to the intrinsic time spread due to the finite length in the z direction of the luminous point. The bunch length affects the resolution in $t_{cl} - R_{cl}/c$ in two ways.

1. The finite luminous point length produces a spread in the collision time of the order of $(\ell/c) \sim 50$ ps, where $\ell \sim 1.5$ cm is the rms spread of the vertex position along z.

2. There is an additional contribution for photons at small angles, also of order $(\ell/c)\cos\theta$ with θ being the polar angle of the photon.

In order to distinguish between these effects, samples of 2γ events at large and small angles have been used. The comparison between the two samples allows us to disentangle the effect (2) since the average $\cos\theta$ for events belonging to the first sample is close to zero. From the analysis of the data we find that most of the constant terms are due to the above effect contributing $\mathcal{O}$ (125 ps), while residual miscalibrations contribute 50 ps. The intrinsic time resolution of the calorimeter is therefore

$$\sigma_t = 54 \text{ ps}/\sqrt{E(\text{GeV})} \oplus 50 \text{ ps}.$$

Use of more data is expected to reduce the constant term.

12.3.3. Analysis of K_L decay and interaction in the calorimeter

The timing capability of the calorimeter is fully exploited in the CP-violation analysis.

As indicated in Fig. 33, the time and positions of the photon clusters together with the K_S direction of flight given by tracking measurements of the
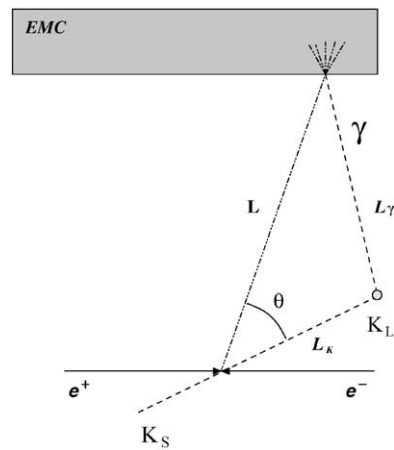

Fig. 33. Determination of the K_L path based on the measurement of time and of position of one photon. In the case of more than one photon, an over-constrained determination can be carried out.
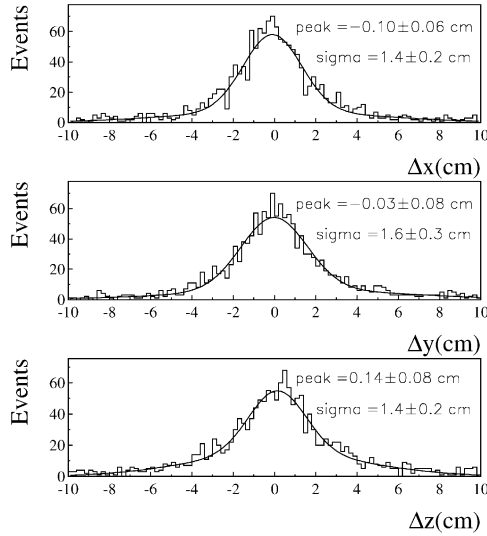
Fig. 34. Difference between the x, y and z coordinates of the $K_L \to \pi^+\pi^-\pi^0$ decay point determined from tracking and calorimeter.

Fig. 35. Velocity spectrum for K_L-mesons interacting in the calorimeter.

$K_S \to \pi^+\pi^-$ decay, determine the K_L-decay vertex position. The resolution for determining a vertex with photons is evaluated using the decay $K_L \to \pi^+\pi^-\pi^0$. The origin of two photons must be the same as that of the vertex of the two charged pions. Fig. 34 shows the distribution of the differences between the coordinates of the two determinations of the decay vertices. The width is dominated by the photon vertex reconstruction resolution since the error from tracking is negligible. A better resolution is expected for the decay $K_L \to \pi^0\pi^0$, where four photons (rather than two) are present. What really matters is the total energy available in photons, 510 MeV for $K_L \to \pi^0\pi^0$ and $\sim 510/3 = 170$ MeV in average for a single π^0 from a three pion decay.

The timing capability of the calorimeter is also useful for K_S tagging by detecting a K_L which reaches the calorimeter. A unique signature of a K_L interaction is provided by the value of β measured from the K_L interaction time, Fig. 35. The low value of β, ~ 0.2, makes its measurement very sensitive to the center of mass energy: the width of the β distribution (see the figure) turns out to be dominated by the intrinsic spread
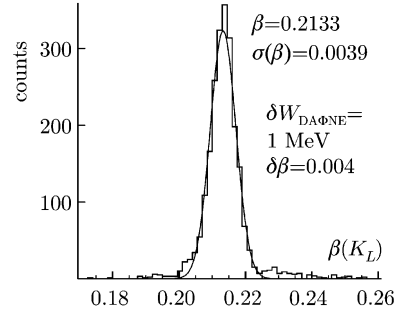
of the machine energy.[9] Thus the measurement of β monitors the variations in the center of mass energy of DAΦNE with an accuracy comparable to that obtained from $K_S \to \pi^+\pi^-$ using the chamber reconstruction of the pion momenta.

12.4. Stability of the time measurements

As mentioned in Section 12.1, 10^6 cosmic ray events allow to evaluate the time offsets with an uncertainty of 50–80 ps and the light velocity in the fibers, v, at the 0.1% level. From the data collected in the period July–December 1999 we reach the following conclusions.

- The measured light velocity is quite stable, Fig. 36.
- Long-time fluctuation of the global time offset t_0^G, Fig. 27, are at the level of few 100 ps. They are due to the changes in DAΦNE provided T_{clk} signal.

These instabilities are completely removed by a continuous calibration. As a benchmark, φ radiative decays accumulated in December 1999 were used. The time residuals, T_{res}, calculated for the two highest energy clusters of the event are shown in Fig. 37. We obtain a stability estimate using the mean of the residuals from data samples of ~ 100 nb^{-1} integrated luminosity, about one day run. The residual rms fluctuation over one month of running time is $\leqslant 30$ ps, as shown in Fig. 37.

---

[9] A center of mass energy spread $\delta W/W \sim 10^{-3}$ results in a spread of β equal to $\delta\beta = (\delta W/W)/(\beta\gamma^2) \sim 4 \times 10^{-3}$.
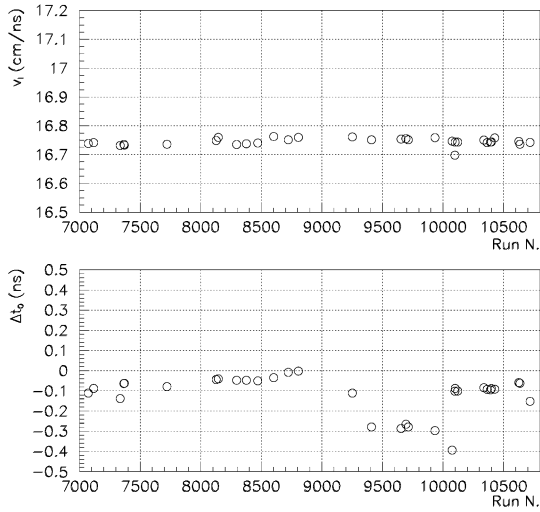
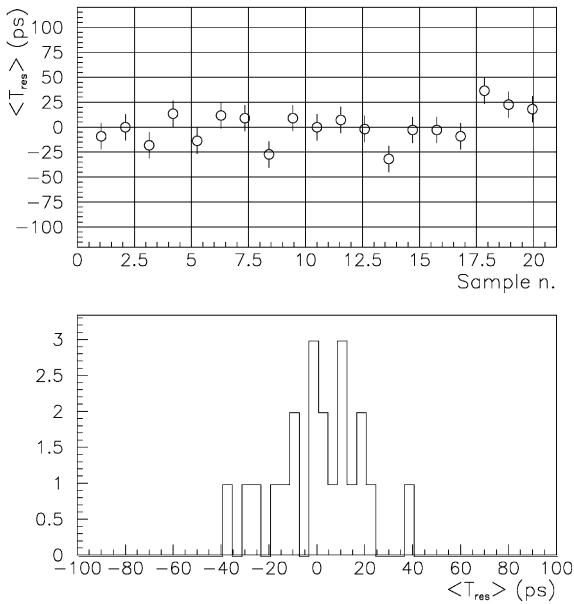Fig. 36. Changes of the measured light velocity and of the average Δt_0 during 1999.

Fig. 37. Top. T_{res} for 100 nb^{-1} of collected data after corrections as a function of the sample number. Bottom. Residual distribution. The rms spread is 18 ps.

13. Photon detection efficiency

The photon detection efficiency can be evaluated using various type of events, we have used the ones listed below.

1. Radiative Bhabha events. Electron and positron momenta and angles from tracking determine the photon direction and energy.
2. $\phi \to \pi^+\pi^-\pi^0$. The energy and direction of one of the two photons are evaluated using the tracking information of the charged pions and the direction of the other photon.
3. $K_L \to \pi^+\pi^-\pi^0$. One photon direction and energy are obtained as above. The π^0 spectrum is similar to the one of interest in CP measurements.

The efficiency is the number of detected cluster divided by the number of produced photons. Clusters are searched in a cone within 3σ's of the expected direction of the photon. The results, in the energy range between 20 and 200 MeV are shown in Fig. 38, and are in reasonable agreement among each other. For energies larger than 100 MeV a constant value of more than 98% is observed. Below 100 MeV we observe a loss in efficiency. This loss is mainly due to the ADC and TDC thresholds. Another effect is due to the clustering algorithm, where a compromise is found between efficiency and background rejection.
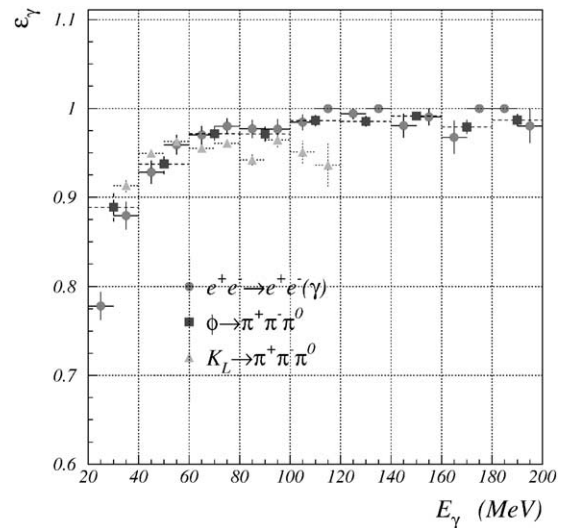

Fig. 38. Photons efficiency vs. energy for $e^+e^- \to e^+e^-\gamma$ events (circles), $\phi \to \pi^+\pi^-\pi^0$ (squares) and $K_L \to \pi^+\pi^-\pi^0$ (triangles).

14. Conclusions

The performance of the KLOE calorimeter has been verified and found very similar to design specifications both with cosmic ray events and with a very limited amount of e^+e^- collision data from DAΦNE. The stringent requirements imposed on the calorimeter by the KLOE physics program can be achieved using a continuous calibration, as was stated in the original proposal and in the following technical proposal [1,2].

The integrated luminosity delivered in 1999, a total of 2.4 pb^{-1} of which 1.8 pb^{-1} collected in the period 24 November–19 December, was barely enough to begin the calibration work. Single cell calibration, for instance, could not be performed with e^+e^- collision data for lack of statistics. Column calibration is performed with e^+e^- collision data and cosmic ray data are used for inter-cell calibration in a column. This is of course more than adequate for the statistics delivered by DAΦNE. Preliminary physics results, using the procedures described in this paper have been presented on various occasions [21–24].

During the past year the DAΦNE luminosity has improved at the cost however of much higher background than originally estimated. 18 pb^{-1} were delivered in November 2000. We have found that the detector, in particular the calorimeter, is quite robust and performs well at high background levels. No offset drifts were observed and accidental overlap of background over good events is less than $\sim 0.1\%$. The main problems that were encountered were related to high trigger rates and limited CPU power.

From the experience accumulated we developed on-line programs for calibration and monitoring the calorimeter operating conditions as well as important DAΦNE parameters. We have been successfully running fully automated calibration procedures, which can be carried out with as little as a few hours of collisions. The calibration constants obtained are entered in a database which is accessed by the reconstruction programs which digest all accumulated data with a delay which can be as low as few hours.

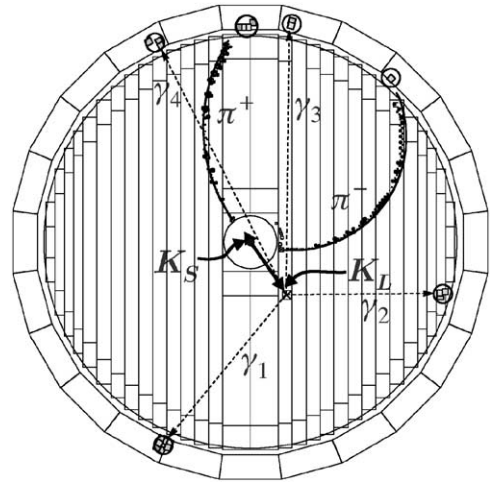An example of the calorimeter function in KLOE is given in Fig. 39. In a $e^+e^- \to \phi \to K_S K_L$

Fig. 39. A CP-violating $\phi \to K_S K_L$ event. The K_S decays into $\pi^+\pi^-$ very close to the interaction point. The K_L decays into $\pi^0\pi^0$ further away resulting in four photons which are detected by the calorimeter.

event, the calorimeter detects the four photons from $K_L \to \pi^0\pi^0$ allowing the reconstruction of the K_L decay and its vertex.

Lomoro, G. Paoluzzi, D. Riondino, A. Rossi and M. Santoni for the realization, test and installation of read-out electronics.

References

[1] KLOE collaboration, KLOE: a general purpose detector for Proposal for DAΦNE, LNF-92/019 (IR) 01.04.1992 (LNF notes are accessible looking at the internet address http://www.lnf.infn.it/sis/reports/searchrep.html.

[2] KLOE collaboration, The KLOE detector—Technical Proposal, LNF-93/002 (IR) 21.01.1993.

[3] S. Guiducci, et al., Proceedings of PAC99, New York, March 1999.

[4] D.W. Hertzog, et al., Nucl. Instr. and Meth. A 294 (1990) 446.

[5] A. Antonelli, et al., Nucl. Instr. and Meth. A 370 (1996) 367.

[6] M. Anelli, et al., Damage induced by light irradiation on blue scintillating fibers, KLOE Note 136 01/95 (KLOE Notes are public and can be accessed looking at the internet addresses http://www.lnf.infn.it/kloe /cgi-bin/list-noteold (KLOE notes from 1 to 136) and http://www.lnf.infn.it/kloe/cgi-bin/listnote.pl (KLOE notes from 137 on)).

[7] M. Anelli, et al., LNF-97/029 (NT).

[8] W.T. Welford, R. Winston, The Optics of Nonimaging Concentrators, Academic Press, New York, 1978.

[9] C. Bini, et al., Optimization study of the KLOE calorimeter light guides, KLOE Note 83/94. A. Di Domenico, A Program for the Simulation of the Winston Cone Light Concentrator, KLOE Note 84/94.

[10] A. Antonelli, et al., Nucl. Instr. and Meth. A 379 (1996) 511.

[11] G. Barbiellini, A. Martinis, F. Scuri, Status Report on the PMT's Mass Test for KLOE, KLOE Note 108, May 1995.

[12] P. Franzini, Errors due to sample time and pile-up, KLOE Note 116, September 1994.

[13] M. Antonelli, et al., Nucl. Instr. and Meth. A 409 (1998) 675.

[14] A. Aloisio, et al., Fast redout system for KLOE, KLOE Note 88/94.

[15] A. Antonelli, et al., Nucl. Instr. and Meth. A 354 (1995) 352.

[16] S. Woelfle, Module zero, analysis of the 1994 test beam at PSI, KLOE Note 134 January 1995.

[17] M. Antonelli, et al., Nucl. Instr. and Meth. A 409 (1998) 558.

[18] C. Bini, et al., Evaluation of the performance of the KLOE calorimeter barrel modules at the cosmic ray stand, KLOE Note 154 02/96.

[19] C. Caso, et al., Eur. J. Phys. 3 (1998) 1.

[20] KLOE Collaboration KLOE first results on hadronic physics, Contributed paper to ICHEP 2000, June 2000, hep-ex/0006036.

[21] KLOE Collaboration First results from $\phi \to K_L K_S$ decays with the KLOE detector, Contributed paper to ICHEP 2000, June 2000, hep-ex/0006035.

[22] KLOE Collaboration, Nucl. Phys. A 663 (2000) 1103.

[23] KLOE Collaboration, The KLOE experiment at DAΦNE, Contributed paper to Chiral Dynamics 2000, June 2000.

[24] KLOE Collaboration KLOE at DAΦNE, Contributed paper to CIPANP 2000, August 2000.